

Experimental and theoretical investigations on the
polymorphism and metastability of BiPO_4 †Cite this: *Dalton Trans.*, 2013, **42**, 14999S. N. Achary,^{*a} D. Errandonea,^b A. Muñoz,^c P. Rodríguez-Hernández,^c F. J. Manjón,^d
P. S. R. Krishna,^e S. J. Patwe,^a V. Grover^a and A. K. Tyagi^a

In this work we report the metastability and the energetics of the phase transitions of three different polymorphs of BiPO_4 , namely trigonal (Phase-I, space group $P3_121$), monoclinic monazite-type (Phase-II, space group $P2_1/n$) and SbPO_4 -type monoclinic (Phase-III, space group $P2_1/m$) from ambient and non-ambient temperature powder XRD and neutron diffraction studies as well as *ab initio* density functional theory (DFT) calculations. The symmetry ambiguity between $P2_1$ and $P2_1/m$ of the high temperature polymorph of BiPO_4 has been resolved by a neutron diffraction study. The structure and vibrational properties of these polymorphs of the three polymorphs have also been reported in detail. Total energy calculations have been used to understand the experimentally observed metastable behavior of trigonal and monazite-type BiPO_4 . Interestingly, all of the three phases were found to coexist after heating a single phasic trigonal BiPO_4 to 773 K. The irreversible nature of these phase transitions has been explained by the concepts of the interplay of the structural distortion, molar volume and total energy.

Received 7th July 2013,
Accepted 5th August 2013
DOI: 10.1039/c3dt51823j

www.rsc.org/dalton

1. Introduction

Crystalline inorganic phosphates have been considered as an important class of materials due to their diversified crystal chemistry under ambient and non-ambient conditions as well as their interesting physical properties amenable for a number of applications. Several of the phosphate lattices, like apatite $[\text{Ca}_{10}(\text{PO}_4)_6\text{X}_2]$, monazite $[\text{M}^{\text{III}}\text{PO}_4]$, cheralite $[\text{M}^{\text{III}}\text{M}^{\text{IV}}(\text{PO}_4)_2]$, zirconium phosphate $[\text{Zr}_2\text{O}(\text{PO}_4)_2]$, NZP $[\text{NaZr}_2(\text{PO}_4)_3]$ etc. have been considered as potential host matrices for the immobilization of radioactive elements separated from high level nuclear

waste (HLW) due to their rock analogous properties *viz.* a high thermal and chemical stability, a high radiation resistant and an insignificant leachability by water.^{1–6} In particular, the orthophosphates of rare-earth ions or alkaline-earth ions are being considered for such applications due to their ion-exchangeability with various radioactive elements. The structures of these phosphates are the key factors in governing their properties for the desired applications.

The crystal structures of phosphates of trivalent cations are largely dependent on their ionic radii, and the structures vary from a silica analogous framework structure to densely packed monazite or zircon-type structures. Rare-earth orthophosphates exist with zircon-type structures for smaller lanthanides and actinides ($\text{Ln} = \text{Gd–Lu}$, Y, Sc, Am, Np, Pu, etc.) and monazite-type structures for larger cations.^{4,7–9} Diversified as well as technologically important functional properties, like microwave dielectric, ionic conduction, low thermal expansion, luminescent, catalytic properties and more importantly immobilization and separation of radioactive nuclides from high level waste (HLW) of nuclear reactors, have been reported for rare-earth phosphates.^{8–15} Similarly, BiPO_4 is considered as a multifunctional material due to its diversified applications, for example it is used as a catalyst and photocatalyst, an ion and humidity sensor, a microwave dielectric, a host for luminescent cations, and in the separation and immobilization of radioactive elements.^{16–23} Furthermore, BiPO_4 exhibits interesting structural features like polymorphism (trimorphic: hexagonal and low (LT) or high (HT) temperature monoclinic form) and morphologies depending on the preparation temperature

^aChemistry Division, Bhabha Atomic Research Centre, Mumbai 400085, India.
E-mail: sachary@barc.gov.in, acharysn@rediffmail.com; Fax: +0091-22-25505151;
Tel: +0091-22-2559 2328

^bMALTA Consolider Team, Departamento de Física Aplicada-ICMUV, Universidad de Valencia, Edificio de Investigación, c/Dr Moliner 50, Burjassot, 46100 Valencia, Spain

^cDepartamento de Física Fundamental II, Instituto de Materiales y Nanotecnología, MALTA Consolider Team, Universidad de La Laguna, La Laguna 38205, Tenerife, Spain

^dInstituto de Diseño para la Fabricación y Producción Automatizada, MALTA Consolider Team, Universitat Politècnica de València, 46022 València, Spain

^eSolid State Physics Division, Bhabha Atomic Research Centre, Mumbai 400085, India

†Electronic supplementary information (ESI) available: (ESI-1). Further details of crystal structural data of the BiPO_4 -I, II and III can be obtained from the Fachinformationszentrum Karlsruhe, Abt. PROKA, 76344 Eggenstein-Leopoldshafen, Germany (fax +49-7247-808-666; E-mail: crysdata@fiz-karlsruhe.de) on quoting the depository CSD numbers 426230 to 426255 (26 structures). See DOI: 10.1039/c3dt51823j

and method.^{24–28} Recently, a large number of studies have been devoted to the preparation of BiPO₄ nanoparticles with a controlled shape and size^{28–30} and in particular on LT-BiPO₄ (monazite-type) due to its luminescence and catalytic properties. Furthermore, much attention has been paid to LT-BiPO₄ due to its preparation simplicity and easy doping of rare-earth ions. Thus, monazite-type BiPO₄ has been used as a co-precipitating agent to recover actinides, in particular plutonium, from HLW of nuclear reactors.^{22,23}

Though there are several reports on the preparation and properties of the BiPO₄ phases, the structural systematic, vibrational properties and high temperature structural behaviors of the three polymorphs are relatively under-explored. The structure and phase transition of BiPO₄ have been reported by Mooney,²⁶ Masse and Durif³¹ and Romero *et al.*³² from X-ray diffraction studies. The low-temperature trigonal polymorph is formed only by controlled low temperature wet chemical processes. It needs to be mentioned here that the structure of the high temperature monoclinic polymorph of BiPO₄ has an ambiguity owing to the contradicting report on the symmetry, *viz.* non-centrosymmetric (*P*₂)²⁶ and centrosymmetric (*P*₂/*m*) lattice.³¹ Interestingly, the structures of all of the polymorphs of BiPO₄ have BiO₈ polyhedra and PO₄ tetrahedra as building blocks but the orientation and nature of the connection of the PO₄ units differs in them. These differences are reflected in the coordination sphere around Bi³⁺ and they are amply reflected in their luminescence properties.^{18,33,34} In order to understand the structural relationship more precisely we have performed neutron diffraction and *in situ* high temperature X-ray diffraction studies on all three polymorphs of BiPO₄. Also, the detailed vibrational properties of the three polymorphs have been investigated by means of Fourier transform infrared (FTIR) absorption and Raman scattering measurements. In addition, the structure and phase transition systematic as well as vibrational properties have been supported by *ab initio* theoretical calculations.

2. Experimental

The BiPO₄ sample was prepared by precipitation from an aqueous solution and subsequent treatments at different temperatures. Bi(NO₃)₃·5H₂O (purity, 98%, Alfa Aesar) and NH₄H₂PO₄ (purity, 98%, Alfa Aesar) were used as the starting materials. The metal content of Bi(NO₃)₃·5H₂O was determined by thermo-gravimetric analyses. Initially, clear solutions of Bi(NO₃)₃·5H₂O in de-ionized water were heated at 333 K on a hot plate. To this hot solution, appropriate amounts of NH₄H₂PO₄ dissolved in de-ionized water were added. A thick white precipitate was formed immediately on the addition of the phosphate solution. The mixture was kept under stirring for about 1 h and then cooled to an ambient temperature and filtered. The residue was washed twice with excess distilled water and then dried at ambient temperature to obtain the trigonal phase of BiPO₄ (I). About 8 g of trigonal-BiPO₄ was heated at 673 K for 5 h in air to obtain the monazite-type

phase (BiPO₄-II). A similar amount of the BiPO₄-I sample was heated at 973 K for 5 h to obtain SbPO₄-type (BiPO₄-III) phase.

All three phases of BiPO₄ were characterized by powder XRD and neutron diffraction studies. The powder XRD patterns at ambient temperature were recorded on a Panalytical X-Pert pro powder X-ray diffractometer using Cu K α radiation. For the powder neutron diffraction study about 6 g of each sample packed in a vanadium can of 1 cm diameter and 5 cm height were used. The incident neutrons with a wavelength of 1.249 Å were used for diffraction experiments. The neutron diffraction data were collected with a linear 5-PSD based Debye–Scherrer type powder diffractometer installed at Dhruva Research Reactor, BARC, Mumbai, in the two-theta range of 5–140°. The total data collection time for each sample was about 24 h. All the powder neutron diffraction and XRD data were analyzed by the Rietveld refinement method using GSAS³⁵ and Fullprof³⁶ software packages.

High-temperature powder XRD patterns of the samples were recorded on the Panalytical X-Pert pro diffractometer using an Anton Par high temperature attachment. A platinum strip was used as a sample holder and heater for the high temperature XRD studies. Slurries of small amounts of well ground samples were smeared on platinum strip. Samples were heated to the desired temperature and held for 2 minutes to get the thermal equilibrium before data collection. The diffraction data were collected in the angular range of 10–80° with a step width and time of 0.02° and 2 s, respectively.

The FTIR absorption spectra of the samples were recorded from 400 to 4000 cm^{−1} on a JASCO Corp. FTIR spectrometer in transmission mode. Thin transparent pellets of a mixture of the sample and KBr were used for the FTIR studies. For the Raman scattering studies, a pre-pressed powder sample (2 mm thick) was placed on a glass slide. Raman measurements were performed in backscattering geometry with a Horiba Jobin Yvon LabRAM HR UV microspectrometer equipped with an edge filter and thermoelectric-cooled multichannel CCD detector. Measurements with a spectral resolution below 2 cm^{−1} were performed using the 632.8 nm line of the HeNe laser for excitation with a laser power below 10 mW to avoid sample heating.

3. Theoretical calculations

Total energy *ab initio* simulations have been performed within the density functional theory (DFT) framework as implemented in the Vienna *ab initio* simulation package (VASP) (see ref. 37 and 38 and references therein). The program performs *ab initio* structural calculations with the plane wave pseudo-potential method. The set of plane waves employed were extended up to a kinetic energy cutoff of 520 eV. Such a large cutoff was required to achieve highly converged results within the projector-augmented-wave (PAW) scheme.^{38,39} The PAW method takes into account the full nodal character of the all-electron charge density distribution in the core region. The exchange-correlation energy was taken in the local density

approximation (LDA)⁴⁰ and in the generalized gradient approximation (GGA) with the revised Perdew–Burke–Ernzerhof (PBESOL) prescription.⁴¹ It is well known that the LDA approach typically overestimates the cohesion energy (producing an underestimation of the equilibrium volume), which is in contrast to the GGA approach which typically underestimates the cohesion energy (producing an overestimation of the equilibrium volume).⁴² We used dense special point grids appropriate to each structure to sample the Brillouin zone (BZ), thus ensuring a high convergence of 1–2 meV per formula unit in the total energy of each structure as well as an accurate calculation of the forces over the atoms. At each selected volume, the structures were fully relaxed to their equilibrium configurations through the calculation of the forces on atoms and the stress tensor.⁴¹ In the relaxed equilibrium configuration, the forces were smaller than $0.006 \text{ eV } \text{\AA}^{-1}$, and the deviation of the stress tensor from a diagonal hydrostatic form was less than 0.1 GPa.

Lattice-dynamic calculations of the phonon modes were performed at the zone center (Γ point) of the BZ. We used a direct force-constant approach (or supercell method)⁴³ as it is conceptually simple. These calculations provide information about the symmetry of the modes and their polarization vectors which allowed us to identify the irreducible representations and the character of the phonon modes at the Γ point. However, this method did not include the contribution from the dipole–dipole interactions resulting in the LO–TO splitting of the infrared-active modes, due to the non-analyticity of this term at the Γ point.

4. Results and discussion

4.1. X-ray and neutron diffraction studies at ambient conditions

The powder XRD patterns of the three phases of BiPO_4 , namely BiPO_4 -I, II and III (shown in Fig. 1) are in agreement with the trigonal, monoclinic monazite-type (JCPDS-PDF-80-0209) and monoclinic high-temperature SbPO_4 type (JCPDS-PDF-77-2208), respectively. The complete transformation from one phase to other and the retention of the transformed phases is a unique example observed in BiPO_4 compared to other orthophosphates of trivalent cations. It has been argued that the water molecules in BiPO_4 play a crucial role in stabilizing the trigonal structure of BiPO_4 -I.³² Such hydrated hexagonal forms have been reported for almost all of the trivalent rare-earth cations and upon dehydration the structure is destabilized and transforms to other structure types.⁴⁴ The comparable coherent neutron scattering lengths of various atoms and negative scattering length of the hydrogen ($b_{\text{O}} = 0.580 \times 10^{-12} \text{ cm}$, $b_{\text{Bi}} = 0.853 \times 10^{-12} \text{ cm}$, $b_{\text{P}} = 0.513 \times 10^{-12} \text{ cm}$, $b_{\text{H}} = -0.374 \times 10^{-12} \text{ cm}$) were helpful to obtain accurate structural parameters by neutron diffraction compared to X-ray diffraction. The detailed structural parameters of the three phases were obtained by Rietveld refinement of the powder neutron diffraction data. The initial structural models for the Rietveld refinements were

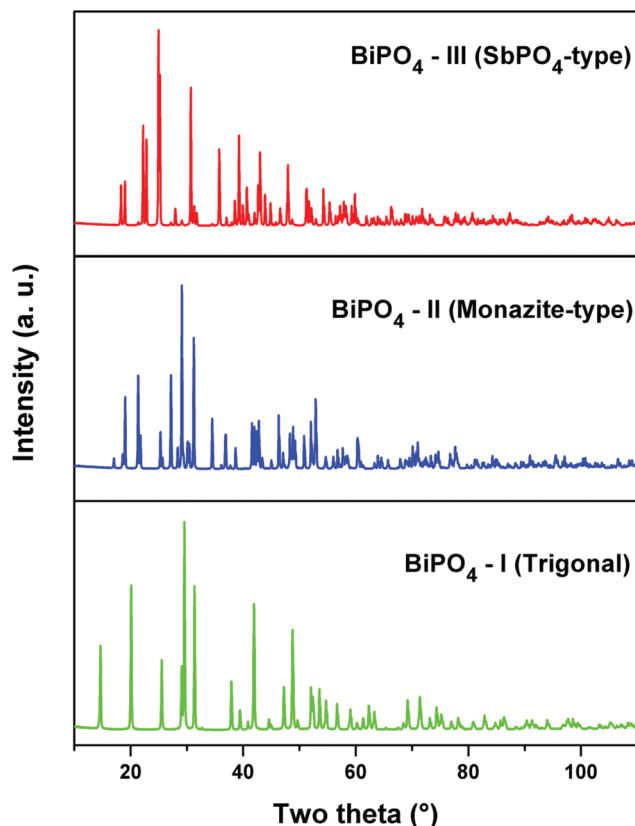


Fig. 1 The powder XRD patterns of the different phases of BiPO_4 at an ambient temperature ($\lambda = 1.5417 \text{ \AA}$).

taken from the structural data reported by Romero *et al.*³² (for trigonal BiPO_4 -I and monazite-type BiPO_4 -II) and Masse and Durif³¹ (for high-temperature BiPO_4 -III). Diffractometer zero and sample displacements parameters were taken from the neutron diffraction pattern of standard Yb_2O_3 . The peaks of the neutron diffraction patterns were computed by using Pseudo-Voigt profile function. The backgrounds of the patterns were fitted with shifted Chebyshev polynomial functions. It can be mentioned here that the background of the neutron diffraction pattern of BiPO_4 -I is drastically different compared to the other two phases which can be attributed to the higher incoherent scattering cross section (80.26 barns) of hydrogen (from water molecule) in this sample. The trigonal BiPO_4 (Phase-I) is a hydrated phase and also contain significant amounts of adsorbed water molecules. From the thermogravimetric (TG) study (see ESI (ESI-1)[†]), it is confirmed that all the water molecules are lost gradually between 323 to 470 K. Beyond 470 K no weight loss is observed and thus the product exists as an anhydrous phase of BiPO_4 . The oxygen (O3) of the trigonal BiPO_4 -I phase represents the lattice water molecule and contributes significantly to the intensities of the Bragg peaks of the neutron diffraction pattern while the adsorbed water molecules contribute only to the background of the diffraction pattern due to incoherent scattering. A refinement of the occupancy of the O3 revealed the non-stoichiometric water molecule in the lattice and the composition of Phase-I as

$\text{BiPO}_4 \cdot 0.67\text{H}_2\text{O}$ (occ. of O3 = 0.335). In order to confirm the symmetry of the lattice, the diffraction data of BiPO_4 -III was also refined on a model structure with space group $P2_1$ proposed by Mooney.²⁶ The obtained results do not show any significant improvement in the residual as well structural parameters compared to the centrosymmetric SbPO_4 -type structural model. The refined parameters for the three phases are given in Tables 1 and 2. The final Rietveld refinement plots for the BiPO_4 phases are shown in Fig. 2(a–c).

The crystal structures of the studied phases of BiPO_4 at an ambient temperature are shown in Fig. 3(a–c). The typical bond lengths and polyhedral parameters in the three different phases of BiPO_4 are given in Table 3. The analyses of the structural parameters of the BiPO_4 phases indicate closely similar tetrahedral PO_4 groups in the three phases. However, the variation in the P–O bond lengths in the trigonal (I) phase are higher than in the other two phases. Furthermore, the dispersion in the P–O bond lengths decreases along the trigonal (I) to monazite (II) to SbPO_4 -type (III) series, which indicates a decreasing trend in the tetrahedral distortion of the PO_4 unit along the transition sequence.

A similar analysis of the Bi–O bond lengths in the three phases shows an abnormal coordination polyhedra around Bi^{3+} in phase-I compared to phases II and III. Six Bi–O bonds in BiPO_4 -I correspond to those in a typical octahedron while two additional bonds at relatively longer distances lead to a highly distorted eight-coordinated BiO_8 polyhedron. The BiO_8 units share their edges forming hexagonal channels along the *c*-axis. The 1-D channels formed in the BiPO_4 -I lattice are occupied by the water molecules (O3) and typical Bi–O(3)_w bond lengths are 3.25 Å. The water molecules provide additional stability to the trigonal structure by reducing the asymmetry of the BiO_8 polyhedra. As the structure transforms to the monazite-type phase (BiPO_4 -II), the BiO_8 unit transforms to a BiO_9 unit due to the cooperative rotation of the PO_4 units. The BiO_9 units consist of eight bonds within 2.36 to 2.70 Å and an additional long bond at 3.02 Å. Furthermore, the SbPO_4 -type (BiPO_4 -III) structure shows highly distorted BiO_8 units which are quite similar to the usual asymmetric coordination

polyhedra due to the lone pair of Bi^{3+} ions. In the BiPO_4 -I, II and III structures, two of the edges of the BiO_n (where $n = 8$ or 9) polyhedra share edges with the PO_4 units to form a linear chain of alternate PO_4 and BiO_n units. In phase-I and III, four other PO_4 units are linked to BiO_8 by sharing corners. However, in phase-II, an additional PO_4 unit comes to close proximity and hence the coordination polyhedra around the Bi^{3+} ion become BiO_9 . The typical linkages of PO_4 and BiO_8 or BiO_9 in these structures are quite similar and they are also closely similar to those in the xenotime-type (or zircon-type) phosphates or vanadates (Fig. 4). Similarly, the BiO_n polyhedra share edges with four other BiO_n units to form linked three dimensional structures. When considering the eight coordinated polyhedra around the Bi^{3+} ions in all of the three structures, it is revealed that the volume of the BiO_8 unit decreases in the BiPO_4 -I ($V_{\text{BiO}_8} = 29.06 \text{ \AA}^3$) to BiPO_4 -II ($V_{\text{BiO}_8} = 26.26 \text{ \AA}^3$) transformation and increases in the BiPO_4 -II to BiPO_4 -III ($V_{\text{BiO}_8} = 27.28 \text{ \AA}^3$) transformation. The observed decrease in the BiO_8 polyhedral volume from phase I to phase II is reflected in the lower unit cell and molar volume of BiPO_4 in phase II. The typical volume per formula units of BiPO_4 in phase-I, II and II are 91.04, 73.77 and 80.61 \AA^3 , respectively. However, the active lone pair present in phase III might be a reason for the metastability of the monazite-type structure compared to the SbPO_4 -type structure. This aspect is further explained in the next section devoted to the high temperature structural studies of the three phases of BiPO_4 . This is also evident from the lower thermal stability of monazite-type BiPO_4 compared to analogous rare-earth phosphates.

4.2. XRD studies at high temperatures

To further understand the stability of the BiPO_4 polymorphs, *in situ* high temperature XRD studies were carried out. The high temperature XRD patterns were recorded at several temperatures in between ambient and 1173 K. At some representative temperatures, the powder XRD patterns of the samples with the BiPO_4 -I, II and -III phases are shown in Fig. 5(a–c). The XRD data collected at different temperatures were

Table 1 The refined unit cell parameters for the different polymorphs of BiPO_4 at an ambient temperature (300 K). (The calculated unit cell parameters are also included for comparison)

	BIPO ₄ -I BiPO ₄ 0.67H ₂ O (trigonal)				BIPO ₄ -II BiPO ₄ (monazite-type)				BIPO ₄ -III BiPO ₄ (SbPO ₄ -type)			
	Space group: $P3_121$ (no. 152)				Space group: $P2_1/n$ (no. 14)				Space group: $P2_1/m$ (no. 11)			
	ND	XRD	LDA	PBESol	ND	XRD	LDA	PBESol	ND	XRD	LDA	PBESol
<i>a</i> (Å)	6.9793(5)	6.9813(2)	6.9151	6.9882	6.7561(4)	6.7552(1)	6.6658	6.7549	4.8807(2)	4.8804(1)	4.7375	4.7809
<i>b</i> (Å)					6.9408(4)	6.9417(2)	6.8869	6.9551	7.0674(3)	7.0684(2)	7.0726	7.1590
<i>c</i> (Å)	6.4743(7)	6.4751(2)	6.3798	6.4314	6.4764(3)	6.4772(2)	6.4148	6.4700	4.7023(2)	4.7033(1)	4.6387	4.7011
β (°)					103.695(5)	103.691(2)	103.79	103.95	96.303(4)	96.285(3)	95.91	96.07
<i>V</i> (Å ³)	273.11(3)	273.31(1)	264.20	272.00	295.06(2)	295.10(1)	286.00	295.00	161.22(1)	161.27(1)	154.6	160.00
<i>Z</i>	3				4				4			
<i>V</i> / <i>Z</i> (Å ³)	91.04				73.77				80.61			
<i>R</i> _p , <i>R</i> _{wp}	0.0164, 0.0216				0.0276, 0.0351				0.0385; 0.0517			
χ^2	0.096				1.073				2.027			
<i>R</i> _F ²	0.0813				0.0578				0.0428			

Table 2 The refined and calculated structural parameters of BiPO₄ at 300 K ((a) trigonal (I), (b) monazite-type (II) and (c) SbPO₄-type (III))

(a) BiPO ₄ -I (trigonal)						
	wyc	x	y	z	Occ	$U_{\text{iso}} (\text{\AA}^2)$
Bi	3b	0.4703(9) 0.47727 0.48136	0 0.00000 0.00000	5/8 0.83333 0.83333	1	0.0077(13)
P	3a	0.4401(15) 0.44011 0.44194	0 0.00000 0.00000	1/3 0.33333 0.33333	1	0.0093(17)
O1	6c	0.3939(12) 0.60625 0.60569	0.1569(15) 0.15651 0.15485	0.4592(10) 0.19788 0.19843	1	0.0231(18)
O2	6c	0.6270(12) 0.49845 0.49651	0.1324(12) 0.12767 0.12678	0.1652(11) 0.49385 0.49308	1	0.0152(17)
O3(w)	6c	0.064(9)*	0.090(10)	0.392(8)	0.335	0.011(5)
1st row: Refined parameters from powder neutron diffraction data. 2nd row: LDA ($a = b = 6.91509 \text{ \AA}$, $c = 6.37979 \text{ \AA}$, $\gamma = 120^\circ$). 3rd row: PBESol. ($a = b = 6.98821 \text{ \AA}$, $c = 6.43141 \text{ \AA}$, $\gamma = 120^\circ$). (Calculated Structures at 0 pressure and 0 K). *Note that in the trigonal structure we neglected the presence of the H ₂ O molecule in calculations.						
(b) BiPO ₄ -II (monazite-type)						
	wyc	x	y	z	Occ	$U_{\text{iso}} (\text{\AA}^2)$
Bi	4e	0.2871(5) 0.2824 0.28394	0.1447(5) 0.1462 0.14513	0.0859(5) 0.0906 0.08817	1	0.0092(6)
P	4e	0.2966(8) 0.2995 0.29933	0.1615(5) 0.1622 0.16215	0.6163(7) 0.6141 0.61291	1	0.0073(9)
O1	4e	0.2617(6) 0.2594 0.25990	0.0003(6) 0.0041 0.00537	0.4459(8) 0.4411 0.44010	1	0.0110(9)
O2	4e	0.3771(6) 0.3799 0.37939	0.3410(7) 0.3422 0.34210	0.5143(6) 0.5148 0.51574	1	0.0067(7)
O3	4e	0.4618(6) 0.4664 0.46480	0.1029(7) 0.1027 0.10182	0.8136(7) 0.8189 0.81782	1	0.0025(8)
O4	4e	0.1161(7) 0.1144 0.11546	0.2011(7) 0.2059 0.20505	0.7097(7) 0.7113 0.70932	1	0.0067(9)
1st row: Refined parameters from powder neutron diffraction data. 2nd row: LDA ($P2_1/n$, setting 7) $a = 6.6658 \text{ \AA}$, $b = 6.8869 \text{ \AA}$, $c = 6.4148 \text{ \AA}$, $\beta = 103.79^\circ$. 3rd row: PBESol. ($P2_1/n$, setting 7) $a = 6.7549 \text{ \AA}$, $b = 6.9551 \text{ \AA}$, $c = 6.4700 \text{ \AA}$, $\beta = 103.95^\circ$. (Calculated structures at 0 pressure and 0 K).						
(c) BiPO ₄ -III (SbPO ₄ -type)						
	wyc	x	y	z	Occ	$U_{\text{iso}}^{\#} (\text{\AA}^2)$
Bi	2e	0.1424(4) 0.12747 0.13160	0.2500 0.25000 0.25000	0.1671(5) 0.15446 0.14926	1	0.00875
P	2e	0.3733(7) 0.63319 0.63746	0.7500 0.25000 0.25000	0.3027(7) 0.67447 0.67464	1	0.00403
O1	2e	0.6761(5) 0.31724 0.32318	0.7500 0.25000 0.25000	0.2291(7) 0.72805 0.72855	1	0.01239
O2	2e	0.6013(6) 0.63648 0.64067	0.2500 0.25000 0.25000	0.3655(6) 0.34423 0.34750	1	0.01373
O3	4f	0.2102(4) 0.20392 0.20006	0.5802(4) 0.57963 0.58078	0.1750(5) 0.18037 0.18053	1	0.01231

Table 2 (Contd.)

(c) BiPO₄-III (SbPO₄-type)**1st row: Refined parameters from powder neutron diffraction data.****2nd row: LDA** ($P2_1/m$, $a = 4.73755 \text{ \AA}$, $b = 7.07260 \text{ \AA}$, $c = 4.63868 \text{ \AA}$, $\beta = 95.91397^\circ$).**3rd row: PBASol.** ($P2_1/m$, $a = 4.78092 \text{ \AA}$, $b = 7.15898 \text{ \AA}$, $c = 4.70108 \text{ \AA}$, $\beta = 96.06833^\circ$).

(Calculated Structures at 0 pressure and 0 K).

#Anisotropic thermal parameters for BiPO₄ (SbPO₄-type).

	$U_{11} (\text{\AA}^2)$	$U_{12} (\text{\AA}^2)$	$U_{13} (\text{\AA}^2)$	$U_{22} (\text{\AA}^2)$	$U_{23} (\text{\AA}^2)$	$U_{33} (\text{\AA}^2)$
Bi	0.0129(13)	0.0	0.0003(9)	0.0022(13)	0.0	0.0110(11)
P	0.0051(16)	0.0	-0.0018(13)	0.0064(15)	0.0	0.0001(17)
O1	0.0014(14)	0.0	-0.0011(13)	0.0262(17)	0.0	0.0092(19)
O2	0.0059(16)	0.0	0.0042(15)	0.0228(19)	0.0	0.0132(19)
O3	0.0134(12)	0.0012(9)	-0.0037(9)	0.0101(12)	-0.0050(10)	0.0124(11)

analyzed by the Rietveld refinement method using the structural parameters as observed in the ambient temperature neutron diffraction studies.

The XRD patterns for BiPO₄-I recorded from ambient temperature to 673 K are almost similar which suggest no structural transition up to 673 K. As mentioned earlier, all the water molecules of BiPO₄-I are lost between 320 to 470 K. The XRD patterns recorded at 573 and 673 K show the presence of only the trigonal phase and thus they can be regarded as the anhydrous trigonal BiPO₄ phase. The XRD patterns of BiPO₄-I recorded up to 473 K represent hydrated phases. Since the loss of water molecules is a gradual process, at different temperatures the composition will have a different water content and thus is non-stoichiometric. As the O3 do not have an appreciable contribution to the XRD patterns compared to that in the neutron diffraction pattern, the exact water contents at different temperatures could not be determined. However, the patterns recorded at 773 K and above show the formation of the BiPO₄-II and III type phases. This observation is in accordance with the structural transitions reported by Romero *et al.*³² and the preparation procedure adopted for this study. It can be mentioned here that the monazite type BiPO₄ (II) could be obtained by heating the trigonal phase at 673 K for 4 h. Earlier, Romero *et al.*³² have mentioned that the trigonal phase transforms to the monazite phase at ambient temperature in about a month. Thus, at a lower temperature the transformation is sluggish and the trigonal to monazite phase transition is kinetically controlled. The analysis of the XRD data of phase I heated at 773 K shows the coexistence of phase-II and III along with phase-I. However the data recorded at 873 and 973 K show the coexistence of only phases II and III. Furthermore, it is observed that the fraction of phase-II gradually decreases when the temperature is increased and completely transforms to phase-III above 973 K. This suggests that phase-III is the only stable phase in BiPO₄ at higher temperatures. A similar analyses of the XRD patterns of BiPO₄-II heated at different temperatures again revealed that phase-II is retained up to 873 K and coexists with phase-III at 973 K. Finally, an analyses of the XRD patterns of BiPO₄-III heated

from ambient temperature to 1173 K do not show any drastic differences. The irreversible nature of the above transitions is further confirmed by the XRD patterns of the samples cooled down to ambient temperature. Thus, the phase-III is the only stable phase of BiPO₄ at higher temperatures and due to its higher structural stability phase-III can be retained at ambient temperatures by cooling the sample from temperatures beyond 973 K. Furthermore, it can be concluded that the trigonal-monazite-SbPO₄ and monazite-SbPO₄ structural transitions depend on the history of the sample and are mainly kinetically controlled. The coexistence of the phases and large volume discontinuity suggests the 1st order nature of all of the transitions. The refined structural parameters at different temperatures and the typical Rietveld refinement plots of phases-I, II, and III are shown in the ESI (ESI-1).†

The variations of the unit cell parameters of the different phases of BiPO₄ with temperature are shown in Fig. 6(a–c). It is observed that the *a*- and *b*-axes of the trigonal BiPO₄-I phase have only a very feeble but noticeable decreasing trend with the increase in temperature up to 473 K and then onward show a positive expansion trend. However, the expansion of the *c*-axis with temperature is related to the edge shared connection of polyhedral (BiO₈ and PO₄) units in the structure (Fig. 4). The unit cell parameters of both the monazite and SbPO₄-type (BiPO₄-II and III) phases show a smooth increasing trend with the increase in temperature, but the monoclinic angle of both of the structures shows a decreasing trend with temperature. The typical thermal expansion coefficients of the different phases of BiPO₄ are: $\alpha_a = 5.6 \times 10^{-6} \text{ K}^{-1}$, $\alpha_c = 11.1 \times 10^{-6} \text{ K}^{-1}$ and $\alpha_v = 22.3 \times 10^{-6} \text{ K}^{-1}$ for BiPO₄-I in between 298–773 K; $\alpha_a = 18.0 \times 10^{-6} \text{ K}^{-1}$, $\alpha_b = 14.5 \times 10^{-6} \text{ K}^{-1}$, $\alpha_c = 10.7 \times 10^{-6} \text{ K}^{-1}$ and $\alpha_v = 44.1 \times 10^{-6} \text{ K}^{-1}$ for BiPO₄-II in between 298–873 K; $\alpha_a = 4.9 \times 10^{-6} \text{ K}^{-1}$, $\alpha_b = 10.7 \times 10^{-6} \text{ K}^{-1}$, $\alpha_c = 14.2 \times 10^{-6} \text{ K}^{-1}$ and $\alpha_v = 32.5 \times 10^{-6} \text{ K}^{-1}$ for BiPO₄-III in between 298–1173 K. In general the edge shared linkages of the polyhedral units are reflected with a higher expansion in the direction of the chains, as in the case of the zircon group materials.^{45–47} Also, they show a lower compressibility along the chain as in the case of the ABO₄ type orthophosphates and

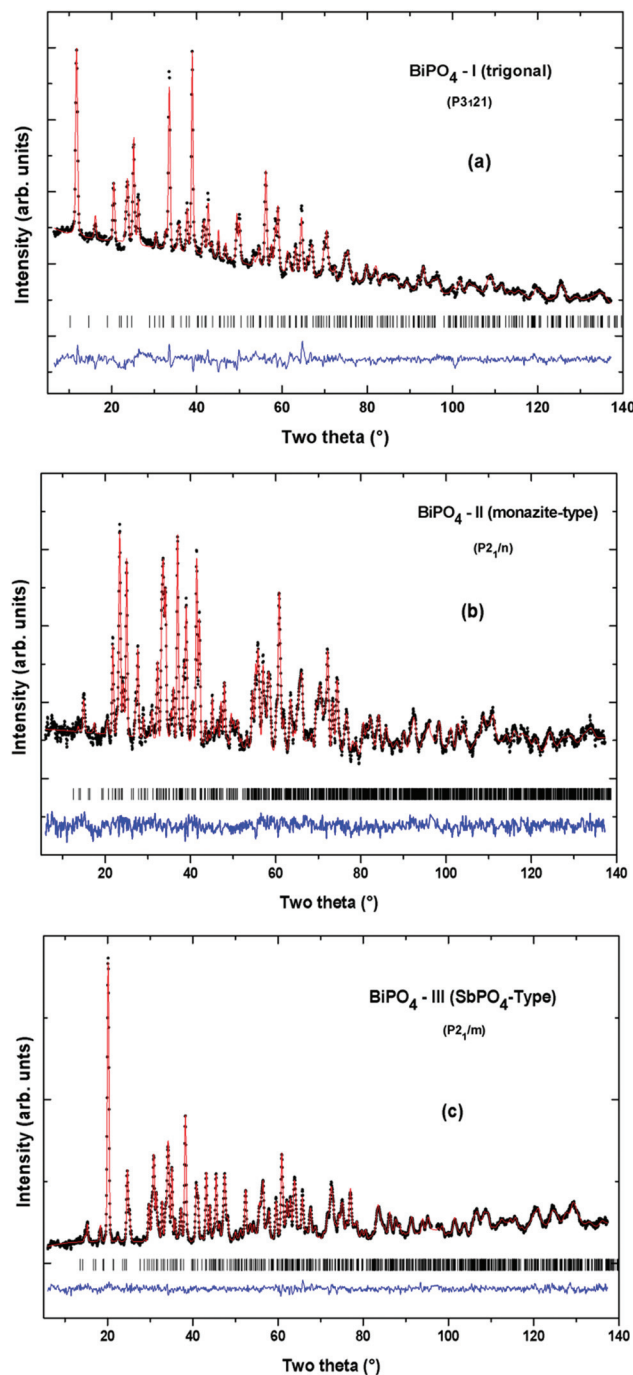


Fig. 2 The Rietveld refinement plots of the powder neutron diffraction data of the BiPO_4 phases, (a) trigonal (I), (b) monazite-type (II) and (c) SbPO_4 -type (III) ($\lambda = 1.249 \text{ \AA}$).

vanadates.^{9,48–51} Furthermore, the differences in the expansion of the BiPO_4 polymorphs are reflected in the variation of the unit volume (V/Z) of BiPO_4 with temperature (Fig. 7). At 773 K, the trigonal to monazite-type structural transformation reduces the volume of the BiPO_4 unit from 95 \AA^3 to 75 \AA^3 , while in the transformation from the trigonal to the SbPO_4 -type structure the volume decreases to about 82 \AA^3 . The more expanded lattice of the SbPO_4 type structure renders more

stability compared to the monazite type phase at higher temperatures and thus the coexistence of these two phases are evident. This observation is supported by first principle total energy calculations explained later in this manuscript. The different trends in the variation of the unit cell parameters of BiPO_4 -I are reflected in the variation of the unit cell volume (Fig. 7). The variation of the molar volume (V/Z) of BiPO_4 -I with temperature shows a feeble decreasing trend up to 473 K. This initial decreasing trend can be assigned to the contraction of the lattice due to the loss of water molecules from the hexagonal channel in the lattice. A subtle positive expansion behavior in between 473 and 673 K can be attributed to the thermal expansion behavior of the anhydrous trigonal BiPO_4 (Phase-I). In a condition, the trigonal, monazite-type and SbPO_4 -type phase can exist with stoichiometry as BiPO_4 and thus they can be regarded as a polymorphic transition.

A detailed analyses of the refined structural parameters of the different polymorphs suggest that the PO_4 tetrahedra are regular in the monazite-type (BiPO_4 -II) and SbPO_4 -type (BiPO_4 -III) phases compared to those in the trigonal phase. The polyhedral characters of the three phases were calculated by IVTON^{52,53} and they are given in Table 4. It can be mentioned here that the PO_4 tetrahedra in the trigonal phase do not act like a rigid unit as is commonly observed in most phosphates. The average bond lengths of P–O of the trigonal phase are also longer compared to the other two phases. A similar analyses of the coordination polyhedra around Bi in the three phases indicate that the BiO_8 or BiO_9 units of the BiPO_4 phases are distorted and asymmetric. Furthermore, the volume distortion⁵³ (the relative difference between the volume of the polyhedra and the volume of the ideal polyhedra expected for a same radius of circumscribed sphere) and eccentricity (the deviation of the central atom position from the ideal centre of the coordination polyhedron) of the BiO_n polyhedra are larger in the trigonal phase compared to the other two phases. The details of the polyhedral analyses of the high temperature structures are given in the ESI (ESI-1)[†]. The larger eccentricity and asymmetry of the trigonal phase is minimized by the additional bonding interaction from the H_2O molecules in the lattice. It is observed that the average Bi–O bond lengths and distortion in the BiO_8 polyhedra increase with the increase in temperature. The increasing trend is significant for the trigonal (I) and monazite (II) type phases compared to the SbPO_4 type phase (III). This result suggests that the SbPO_4 type phase is the stable phase for BiPO_4 at ambient conditions. The relatively expanded lattice can be attributed to the higher stability of the SbPO_4 -type phase. In the next section we further study the stability of these phases by means of *ab initio* theoretical calculations.

4.3. Total energy *ab initio* calculations

The zero pressure and temperature unit cell parameters and position coordinates of the three different phases of BiPO_4 (I, II and III) as calculated by LDA and PBEsol approaches are given in Tables 1 and 2, which indicate a close agreement in

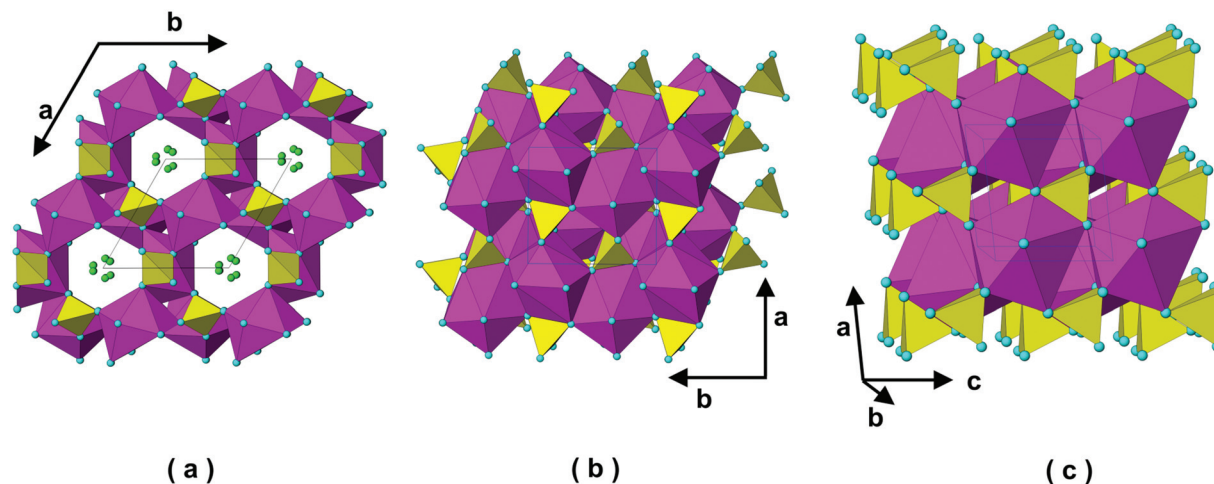


Fig. 3 The crystal structure of the BiPO_4 phases. (a) Trigonal (I), (b) monazite-type (II) and (c) SbPO_4 -type (III). (BiO_8 (in a and c), BiO_9 (in b) and PO_4 units are shown). The isolated spheres are O3 (of water molecules in BiPO_4 -I).

Table 3 The typical bond lengths and polyhedral parameters in the different phases of BiPO_4

BiPO_4 -I (trigonal)		BiPO_4 -II (monazite-type)		BiPO_4 -III (SbPO_4 -type)	
Bi–O1	2.817(8) (Å)	Bi–O1	2.580(6) (Å)	Bi–O1	2.149(4) (Å)
Bi–O1	2.296(8)	Bi–O1	2.492(5)	Bi–O1	2.880(4)
Bi–O1	2.817(7)	Bi–O2	3.020(5)	Bi–O2	2.896(4)
Bi–O1	2.296(12)	Bi–O2	2.399(6)	Bi–O2	2.330(3)
Bi–O2	2.378(7)	Bi–O2	2.700(5)	Bi–O3	2.357(3)
Bi1–O2	2.490(9)	Bi–O3	2.361(6)	Bi–O3	2.526(3)
Bi–O2	2.490(7)	Bi–O3	2.394(6)	Bi–O3	2.526(3)
Bi–O2	2.378(8)	Bi–O4	2.469(5)	Bi–O3	2.357(3)
		Bi–O4	2.426(6)		
CN:	6 + 2	CN	8 + 1	CN	8
<Bi–O>	2.495(3) (Å)	<Bi–O> ₉	2.538(2) (Å)	<Bi–O>	2.503(1) (Å)
Distt.	62.976×10^{-4}	Distt.	60.598×10^{-4}	Distt.	98.915×10^{-4}
		<Bi–O> ₈	2.478(2) (Å)		
		Distt.	18.238×10^{-4}		
V_{BiO_8} (Å ³)	29.06	V_{BiO_8} (Å ³)	26.26	V_{BiO_8} (Å ³)	27.28
Distt.	0.1491	Distt.	0.0684	Distt.	0.0819
Sphericity	0.844	Sphericity	0.941	Sphericity	0.910
Eccentricity	0.346	Eccentricity	0.196	Eccentricity	0.449
		V_{BiO_9} (Å ³)	31.95		
		Distt.	0.0557		
		Sphericity	0.853		
		Eccentricity	0.308		
P–O1	1.523(12) (Å)	P–O1	1.550(7) (Å)	P–O1	1.554(4) (Å)
P–O1	1.523(9)	P–O2	1.567(7)	P–O2	1.552(4)
P–O2	1.592(9)	P–O3	1.539(6)	P–O3	1.526(3)
P–O2	1.592(10)	P–O4	1.509(8)	P–O3	1.526(3)
<P–O> ₄	1.558(5) (Å)	<P–O> ₄	1.541(4) (Å)	<P–O>	1.540(2) (Å)
Distt.	4.895×10^{-4}	Distt.	1.839×10^{-4}	Distt.	0.757×10^{-4}
V_{PO_4} (Å ³)	1.923	V_{PO_4} (Å ³)	1.862	V_{PO_4} (Å ³)	1.861
Distt.	0.0128	Distt.	0.0094	Distt.	0.0070
Sphericity	1	Sphericity	1	Sphericity	1
Eccentricity	0.042	Eccentricity	0.066	Eccentricity	0.116

both calculations with the experimental results. It may be noted here that the H_2O molecules of the trigonal (I) phase are neglected in both calculations. As the hydrated and anhydrous form of the trigonal BiPO_4 (Phase-I) are structurally equivalent except for the occupancy of O3, a direct comparison of the total energy of the three polymorphs can be made without considering water molecules. The calculated total energy (E) as

a function of the volume for the three different phases of BiPO_4 as observed by PBESol and LDA are shown in Fig. 8. A comparison of the calculated unit cell parameters with the corresponding experimentally observed values indicates a close agreement in the case of PBESol compared to LDA. As mentioned earlier, the LDA approximation in general underestimates the equilibrium volume due to the overestimation of

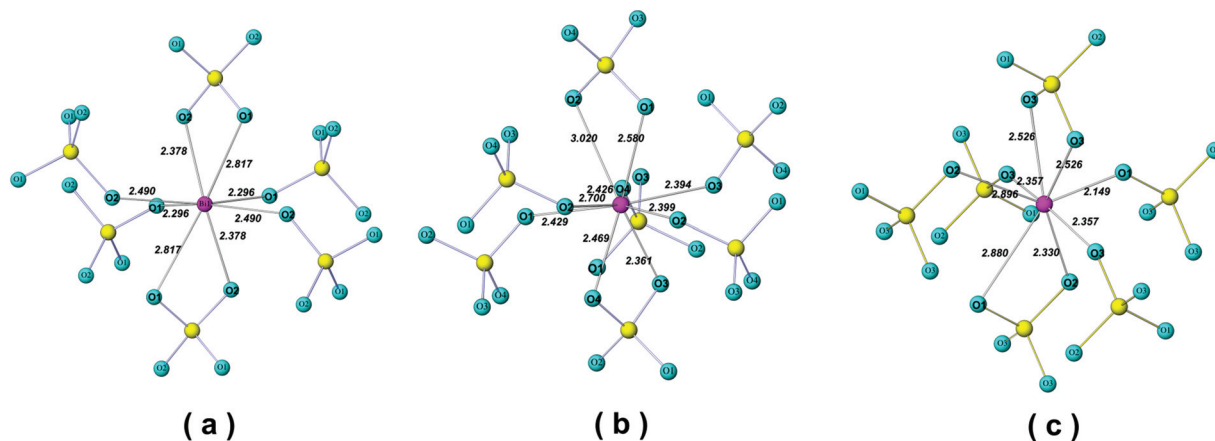


Fig. 4 The typical coordination around Bi^{3+} in the BiPO_4 phases. (a) Trigonal (I), (b) monazite type (II) and (c) SbPO_4 type (III).

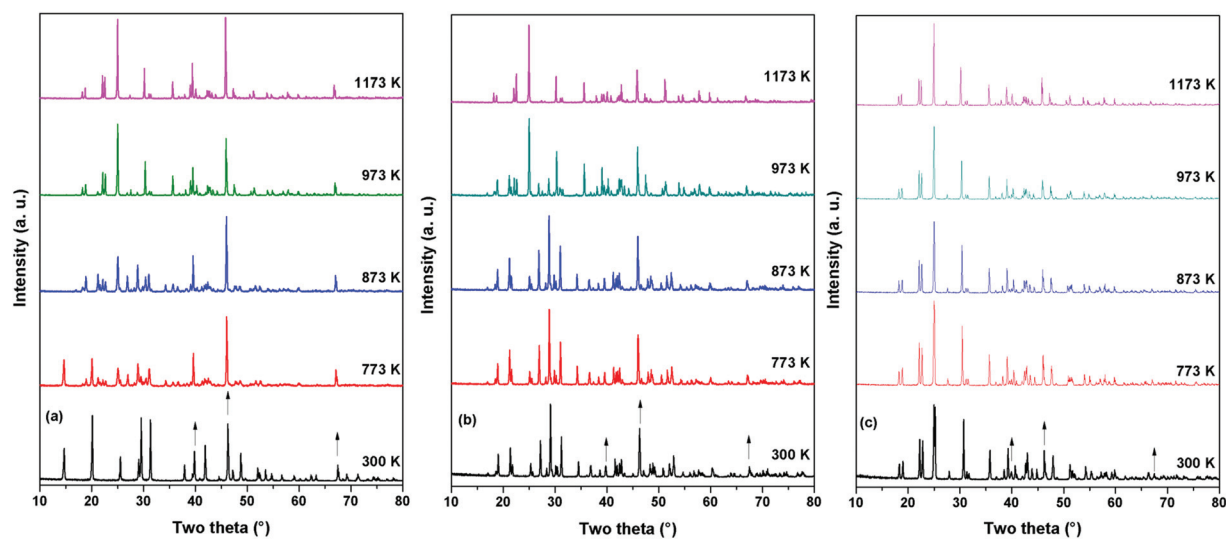


Fig. 5 Powder XRD patterns of the BiPO_4 phases at representative temperatures. (a) Trigonal (I), (b) monazite-type (II) and (c) SbPO_4 -type (III) (\dagger indicates the platinum sample holder base peaks).

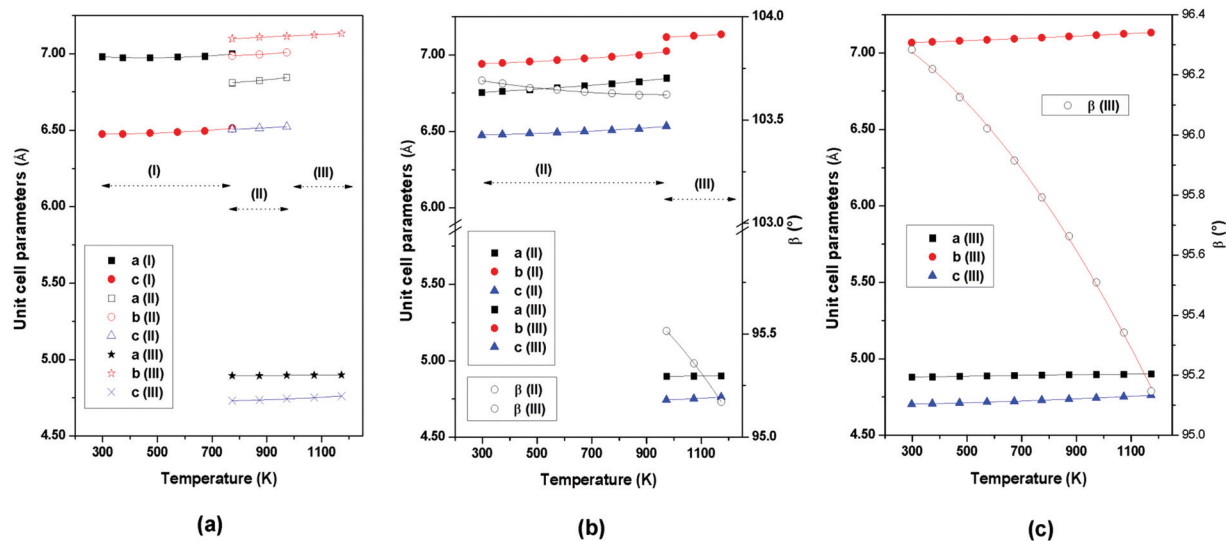


Fig. 6 The variation of the unit cell parameters of BiPO_4 with temperature. (a) Trigonal (I), (b) monazite-type (II) and (c) SbPO_4 -type (III).

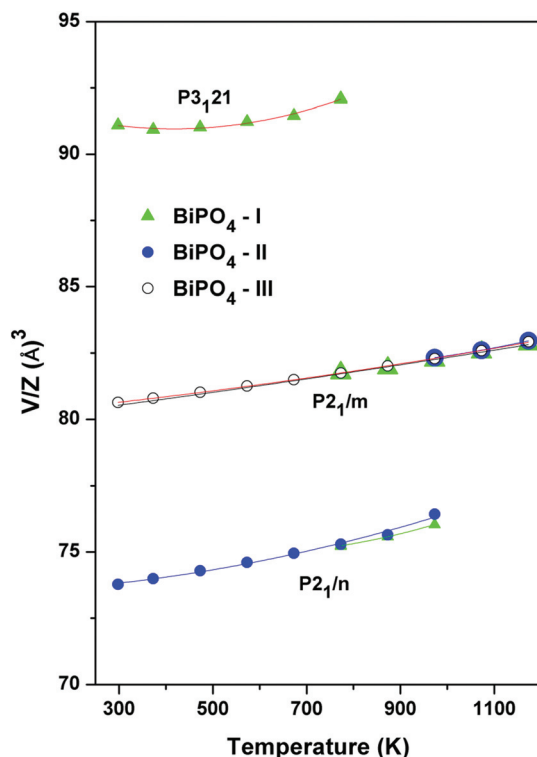


Fig. 7 The variation of the molar volume of the BiPO_4 phases with temperature.

the cohesion energy, while the GGA approximation over estimates the equilibrium volume due to the underestimation of the cohesion energy.⁴² In the present case, the unit-cell volumes calculated by LDA are about 3% lower while the same calculated by PBESol are in agreement within 0.5%. The position coordinates calculated by both approximations are in agreement within 3%. According to the total energy calculated by the PBESol approximation both the monazite- and SbPO_4 -type structures are stable at ambient conditions while that calculated by LDA suggests that the monazite-type structure has a little higher stability (Fig. 8). The metastable nature of the trigonal phase can be clearly concluded from the large differences in the lattice energy from the other structure types. The total energy of BiPO_4 -II (monazite-type) and BiPO_4 -III (SbPO_4 -type) observed by PBESol are comparable while that obtained by LDA show only a marginal higher value for phase-III compared to phase-II. This suggests that the SbPO_4 - and monazite-type lattices have a competing stability in the case of BiPO_4 .

The volume dependence of the energy indicates that the increase in the volume will favor the SbPO_4 -type structure compared to the monazite phase. Thus at a higher temperature, the SbPO_4 -type phase would be the expected stable phase for BiPO_4 as observed from the high temperature XRD studies. This can be seen in Fig. 8, where if the molar volume exceeds above 75 \AA^3 (150 \AA^3 in Fig. 8) the total energy of the monazite structure becomes higher than that of the SbPO_4 -type structure favoring the transformation towards the last phase. Fig. 8 also indicates that upon volume reduction

Table 4 The calculated and observed infrared modes of the different BiPO_4 phases. ((a) trigonal (I), (b) monazite-type (II) and (c) SbPO_4 -type (III))

(a) Trigonal (BiPO_4 -I)

Mode	LDA ω (cm^{-1})	Mode	PBESol ω (cm^{-1})	Mode	Exp. ω (cm^{-1})
E(RI)	68.414	E(RI)	64.4806		
A2(I)	81.590	A2(I)	78.057		
E(RI)	90.897	E(RI)	87.931		
A2(I)	104.940	A2(I)	106.544		
E(RI)	116.314	E(RI)	107.578		
E(RI)	146.135	A2(I)	139.669		
A2(I)	147.536	E(RI)	142.2376		
E(RI)	157.944	E(RI)	156.448		
E(RI)	191.967	E(RI)	187.203		
A2(I)	205.210	A2(I)	195.776		
E(RI)	223.289	E(RI)	214.890		
E(RI)	247.906	E(RI)	240.042		
A2(I)	251.242	A2(I)	241.844		
E(RI)	355.281	E(RI)	351.190		
E(RI)	464.691	E(RI)	456.668	E(RI)	443b
E(RI)	508.088	E(RI)	503.035		
A2(I)	533.472	A2(I)	526.886	A2(I)	539s
E(RI)	554.754	E(RI)	548.035	E(RI)	553w
A2(I)	570.131	A2(I)	563.846	A2(I)	560w
E(RI)	575.401	E(RI)	568.750	E(RI)	594s
E(RI)	944.692	E(RI)	928.447		
E(RI)	964.640	E(RI)	946.861	E(RI)	949s
A2(I)	982.452	A2(I)	964.907		
E(RI)	985.354	E(RI)	968.176	E(RI)	957s
A2(I)	1017.977	A2(I)	996.597		
E(RI)	1068.679	E(RI)	1047.101	E(RI)	1023s
					1065s

(b) Monazite-type (BiPO₄-II)

Mode	LDA ω (cm ⁻¹)	Mode	PBESol ω (cm ⁻¹)	Mode	Exp. ω (cm ⁻¹)
Au(I)	71.850	Au(I)	65.915		
Bu(I)	83.258	Bu(I)	75.555		
Au(I)	86.527	Au(I)	83.395		
Bu(I)	112.812	Bu(I)	102.976		
Au(I)	124.053	Au(I)	112.116		
Bu(I)	154.208	Bu(I)	147.041		
Au(I)	157.143	Au(I)	154.447		
		Bu(I)	172.493		
Au(I)	179.859	Au(I)	174.495		
Bu(I)	180.059				
Bu(I)	194.436	Bu(I)	188.305		
Au(I)	208.746	Au(I)	203.716		
Bu(I)	217.652	Bu(I)	213.757		
Au(I)	236.999	Au(I)	227.967		
		Au(I)	254.186		
		Bu(I)	256.421		
Bu(I)	260.915				
Au(I)	262.483				
Bu(I)	366.722	Bu(I)	359.430		
Au(I)	368.957	Au(I)	363.934		
Au(I)	455.618	Au(I)	449.496		
Bu(I)	470.295	Bu(I)	463.373	Bu(I) + Bu(I)	473w
Au(I)	502.284	Au(I)	497.932		
Bu(I)	519.996	Bu(I)	514.844		
Au(I)	528.802	Au(I)	523.784	Au(I)	529s
Bu(I)	539.276	Bu(I)	533.091	Bu(I)	554s
Bu(I)	567.996	Bu(I)	562.579	Bu(I)	564s
Au(I)	583.440	Au(I)	576.756	Au(I)	604s
Bu(I)	919.141	Bu(I)	898.993	Bu(I)	876w
Au(I)	927.614	Au(I)	908.867		
Au(I)	937.154	Au(I)	917.306		
Bu(I)	941.690	Bu(I)	922.276	Bu(I)	930s
Bu(I)	975.847	Bu(I)	960.671	Bu(I)	958s
Au(I)	981.151	Au(I)	963.974		
Bu(I)	1041.426	Bu(I)	1023.317	Bu(I)	1011s
Au(I)	1052.968	Au(I)	1033.925	Au(I)	1031s
					1076s

(c) SbPO₄-type (BiPO₄-III)

Mode	LDA ω (cm ⁻¹)	Mode	PBESol ω (cm ⁻¹)	Mode	Exp. ω (cm ⁻¹)
Bu(I)	120.184	Bu(I)	109.080		
Au(I)	126.955	Au(I)	113.516		
Bu(I)	153.507	Bu(I)	149.909		
Au(I)	185.196	Au(I)	182.7673		
Bu(I)	201.340	Bu(I)	196.410		
Au(I)	209.880	Au(I)	203.616		
Au(I)	322.725	Au(I)	320.468		
					421w
					434w
					451w
					457w
Bu(I)	481.869	Bu(I)	474.848	Bu(I)	472w
Au(I)	494.545	Au(I)	491.860	Au(I)	494s
Bu(I)	508.088	Bu(I)	503.702	Bu(I)	513s
					527w
Bu(I)	582.373	Bu(I)	576.222	Bu(I)	554s
					630s
Au(I)	933.651	Au(I)	913.670		
Bu(I)	936.120	Bu(I)	918.707	Bu(I)	928w
				Bu(I)	963s
Bu(I)	1003.333	Bu(I)	987.624	Bu(I)	1005s
Bu(I)	1048.631	Bu(I)	1029.521	Bu(I)	1029s
					1105s

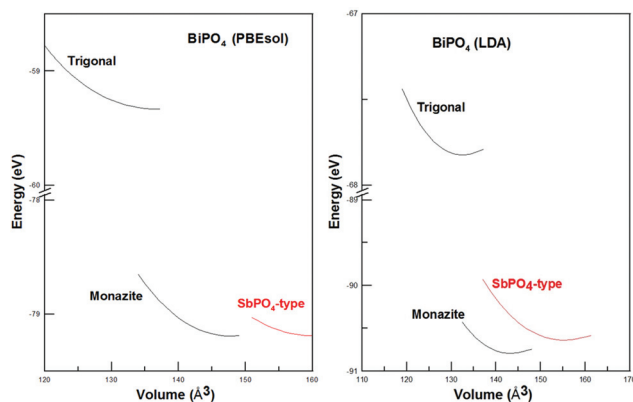


Fig. 8 The total energy as calculated by the LDA and PBESol approach.

(compression) the SbPO_4 -type BiPO_4 will transform into monazite at a relative low pressure. In the trigonal structure, the large unit-cell volume of BiPO_4 is mainly stabilized by the water molecules. As the water molecules are lost, the larger total energy destabilizes the system and collapses to the nearest volume and energy structures. This explains the coexistence of phases I, II and III that we observed at 773 K. Similar arguments can be used to support the coexistence of phases II and III at higher temperatures. Finally, the complete transformation occurs at 1073 K because of the aforementioned reasons.

4.4. FTIR absorption and Raman scattering studies at ambient conditions

The differences between the polymorphs of BiPO_4 are evidenced by the Raman and infrared spectroscopic measurements. The FTIR absorption and Raman spectra of the BiPO_4 -I, II and III polymorphs are shown in Fig. 9 and 10. According to group theory and site symmetry analyses 54, 72 and 36 vibrational modes are expected for BiPO_4 -I, II and III, respectively. The corresponding irreducible representations are:

BiPO_4 -I ($P3_121$) $\Gamma = 8A_1 + 9A_2 + 35E$ (assuming no water molecules)
 $9A_2 + 17A_2$ (are IR active) and $8A_1 + 18E$ (are Raman Active)

BiPO_4 -II ($P2_1/n$) $\Gamma = 18A_g + 17A_u + 18B_g + 16B_u$

BiPO_4 -III ($P2_1/m$) $\Gamma = 11A_g + 6A_u + 7B_g + 9B_u$

where, the u modes are IR active and the g modes are Raman active for both the monazite type and SbPO_4 type structures.

Ab initio calculated IR- and Raman-active mode frequencies (both with LDA and PBESol) for the three phases of BiPO_4 are given in Tables 4(a-c) and 5(a-c), respectively, and marked with vertical arrows in Fig. 9 and 10. In order to compare the local coordination of the three polymorphs, the stoichiometric composition BiPO_4 for all of the three phases is considered for the calculations. The calculated mode frequencies can be compared to the IR- and Raman-active modes determined experimentally and a rather good agreement is found. The vibrational modes of the Bi-O bonds in the BiO_n units are calculated and observed at low frequencies (*i.e.* below 250 cm^{-1})

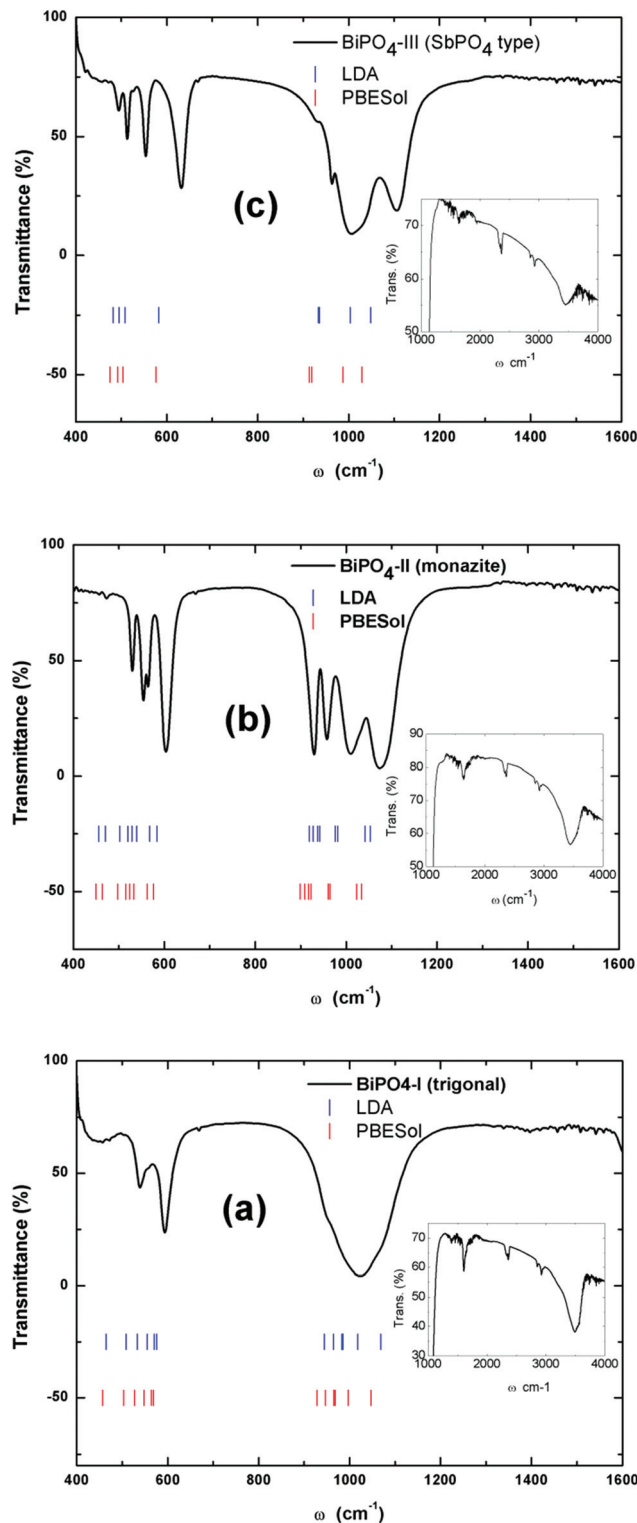


Fig. 9 Typical FTIR spectra of BiPO_4 phases. (a) Trigonal (I), (b) monazite-type (II) and (c) SbPO_4 -type (III). Vertical ticks indicate the calculated frequencies.

in the IR measurements,^{54,55} and they are beyond the measurement range. Thus, only higher frequencies modes, which are characteristic of the tetrahedral PO_4 units are used to identify the differences in the structures.

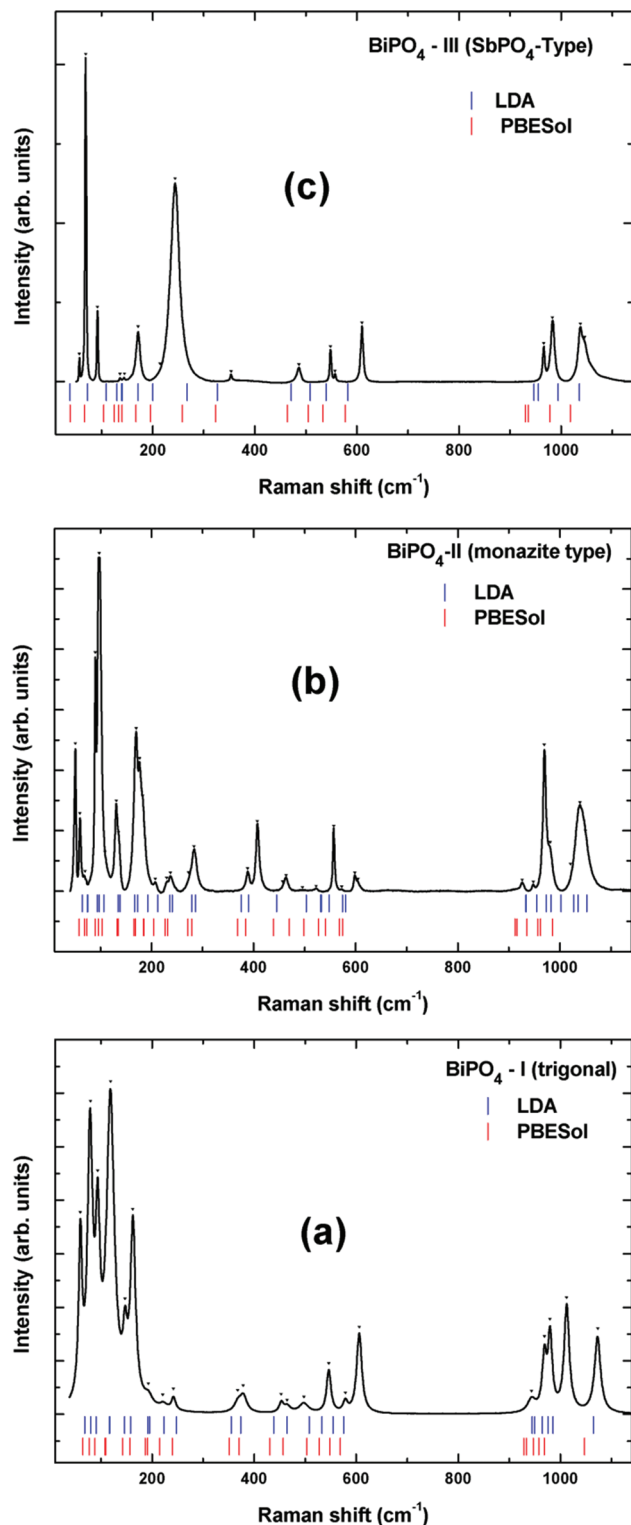


Fig. 10 Typical Raman spectra of BiPO_4 phases. (a) Trigonal (I), (b) monazite-type (II) and (c) SbPO_4 -type (III). Vertical ticks indicate the calculated frequencies.

It is known that the isolated tetrahedral PO_4 group has T_d symmetry and has four internal vibrational modes ($A_1 + E + 2F_2$), all being Raman-active but only F_2 modes being

IR-active.⁵⁶ The A_1 and one of the triply degenerated F_2 modes are due to the symmetric (ν_1) and asymmetric (ν_3) stretching modes of the P–O bonds in the PO_4 units. On the other hand, the doubly degenerated E mode (ν_2) and the other F_2 mode (ν_4) correspond to the O–P–O bending modes of the PO_4 units. These modes are located at 938 (ν_1), 420 (ν_2), 1017 (ν_3) and 567 cm^{-1} (ν_4) for the isolated PO_4 group.⁵⁷ The recorded IR spectrum of BiPO_4 -I shows broad overlapping bands between 949 and 1065 cm^{-1} (ν_3 bands), distinct bands at 539 and 594 cm^{-1} and weak bands at 553 and 560 cm^{-1} (ν_4).¹⁹ In addition, the enhanced bands at higher frequencies, *viz.* 1611 and 3475 cm^{-1} are due to the characteristic H–O–H bending and O–H stretching modes of the water molecules present in BiPO_4 -I. A shoulder around 3550 cm^{-1} can be accounted to the stretching of the H–O–H bonds of adsorbed water or non-associated water molecules. These bands are practically absent in the other two phases (or reduced to a minimum due to the contribution of the adsorbed H_2O in the experimental environment). As the structure undergoes transformation, the site symmetry of the PO_4 group changes from C_2 , C_1 and t_d and thus the IR bands due to the PO_4 units appear as differently split bands. Due to the larger distortion in the PO_4 units of BiPO_4 -I, a number of overlapped peaks leads to a broad band. Furthermore, due to the lowering of the local symmetry of the PO_4 units in BiPO_4 -II, a larger number of bands, *viz.* 1076, 1031, 1011, 958, 930, 604, 564, 554 and 529 cm^{-1} , are observed. These bands are similar to those reported earlier for monazite-type BiPO_4 .¹⁹ Comparing the earlier reported vibrational modes, the bands 1075, 1010 and 958 cm^{-1} can be assigned to the asymmetric (ν_3) stretching modes and the band at 930 cm^{-1} can be assigned to the symmetric (ν_1) stretching mode of the PO_4 units. The low-frequency bands (ν_4) at 605, 565, 553 and 530 cm^{-1} are due to the bending modes of the O–P–O links. Similarly, IR bands were observed in BiPO_4 -III at 1105, 1029, 1005, 963 (ν_3 bands), 928 (ν_1), 554, 527, 513 and 494 (ν_4 bands) cm^{-1} . Additional new bands at 669 and 632 cm^{-1} might be arising from the ν_3 and ν_1 modes of the PO_4 units.

With regards to the Raman scattering measurements of the BiPO_4 polymorphs presented in Fig. 10, it must be emphasized here that the Raman data of BiPO_4 already reported in the literature are obscure in its interpretation, though they have been often used to characterize the BiPO_4 phases.^{16–19,32,58,59} In most cases, the high-frequency Raman modes of free PO_4 units were used to characterize the different phases, but a complete mode analysis has not been undertaken to our knowledge. Here we present a detailed symmetry analysis and computational study which has allowed us to identify almost all of the Raman modes of the BiPO_4 phases (see Table 5(a–c)). In the present study, about 20 modes could be clearly identified in the Raman spectra of BiPO_4 -I. As expected, internal vibrational modes of the PO_4 units appear at high frequencies, while those due to the internal modes of the BiO_8 units are observed at a low frequency. The intense A_1 (118.7 cm^{-1} , strong and sharp) and E (241.7 cm^{-1} , strong and broad) modes are due to the internal modes of the BiO_8 polyhedra in

Table 5 The calculated and observed Raman modes of the BiPO₄ phases. ((a) Trigonal (I), (b) monazite-type (II) and (c) SbPO₄-type (III))

(a) Trigonal (BiPO ₄ -I)					
Mode	LDA ω (cm ⁻¹)	Mode	PBESol ω (cm ⁻¹)	Modes	Exper. ω (cm ⁻¹)
E(RI)	68.414	E(RI)	64.480		
A1(R)	79.922	A1(R)	77.223		
E(RI)	90.897	E(RI)	87.931	E(RI)	93.6
E(RI)	116.314	E(RI)	107.578		
A1(R)	117.148	A1(R)	109.780	A1(R)	118.7
E(RI)	146.135	E(RI)	142.237	E(RI)	146.9
E(RI)	157.944	E(RI)	156.448	E(RI)	162.2
E(RI)	191.967	E(RI)	187.203	E(RI)	192.6
A1(R)	195.303	A1(R)	191.273		
E(RI)	223.289	E(RI)	214.890	E(RI)	220.8
E(RI)	247.906	E(RI)	240.042	E(RI)	241.7
E(RI)	355.281	E(RI)	351.190	E(RI)	367.9
A1(R)	373.494	A1(R)	370.705	A1(R)	378.8
A1(R)	438.506	A1(R)	430.515	A1(R)	452.8
E(RI)	464.691	E(RI)	456.668	E(RI)	464.7
E(RI)	508.088	E(RI)	503.035	E(RI)	497.5
A1(R)	532.938	A1(R)	527.186	A1(R)	546.4
E(RI)	554.754	E(RI)	548.035	E(RI)	579
E(RI)	575.401	E(RI)	568.750	E(RI)	606.2
E(RI)	944.692	E(RI)	928.447	E(RI)	943.7
A1(R)	949.162	A1(R)	933.217		
E(RI)	964.640	E(RI)	946.861	E(RI)	968.8
A1(R)	975.881	A1(R)	957.735	A1(R)	979.7
E(RI)	985.354	E(RI)	968.176	E(RI)	1012
E(RI)	1068.679	E(RI)	1047.101	E(RI)	1073.4
(b) Monazite-type (BiPO ₄ -II)					
Mode	LDA ω (cm ⁻¹)	Mode	PBESol ω (cm ⁻¹)	Mode	Exper. ω (cm ⁻¹)
Ag(R)	64.378	Ag(R)	58.209	Ag	50.9
Ag(R)	74.285	Ag(R)	68.383	Ag	59.8
Bg(R)	75.286	Bg(R)	73.287	Bg	69.9
Bg(R)	93.699	Bg(R)	89.332	Bg	89.6
Ag(R)	97.335	Ag(R)	95.337	Ag	97.3
Bg(R)	106.908	Bg(R)	102.642	Bg	108.6
		Ag(R)	132.697	Bg	131.1
Bg(R)	134.561	Bg(R)	134.732	Bg	135.5
Ag(R)	138.597				
Ag(R)	166.950	Ag(R)	165.688	Ag	169.9
Bg(R)	172.921	Bg(R)	167.790	Bg + Ag	176.7
Ag(R)	172.787	Ag(R)	168.424		
Ag(R) + Bg(R)	192.601	Ag(R)	184.002	Ag + Bg	182.7
		Bg(R)	185.236		
Bg(R)	212.115	Bg(R)	203.883	Bg	207.4
Bg(R)	235.931	Bg(R)	226.199	Bg	229.8
Ag(R)	240.434	Ag(R)	231.903	Ag	237.1
Bg(R)	279.095	Bg(R)	271.332	Bg	272.5
Ag(R)	286.133	Ag(R)	278.671	Ag	283.5
Bg(R)	375.729	Bg(R)	368.303	Bg	388.4
Ag(R)	390.439	Ag(R)	384.549	Ag	407.4
Ag(R)	445.077	Ag(R)	438.688	Ag	457.0
Bg(R)	477.833	Bg(R)	469.945	Bg	463.5
Ag(R)	503.051	Ag(R)	497.999	Ag	495.9
Ag(R)	531.404	Ag(R)	527.220	Ag	522.7
Bg(R)	532.638	Bg(R)	527.287	Bg	557.1
Bg(R)	547.749	Bg(R)	540.930	Bg	572.6
Ag(R)	573.867	Ag(R)	568.083	Ag	598.3
Bg(R)	580.405	Bg(R)	573.921	Bg	604.5
Ag(R)	933.184	Ag(R)	911.936	Ag + Bg	926.3
Bg(R)	933.685	Bg(R)	915.772		
Ag(R)	954.933	Ag(R)	935.286	Ag	947.8
Ag(R)	973.412	Ag(R)	956.502	Ag	969.5
Bg(R)	982.552	Bg(R)	962.272	Bg	981.0
Bg(R)	1001.799	Bg(R)	985.256	Bg	1021.0
Ag(R)	1027.383	Ag(R)	1010.141	Ag	1039.4
Bg(R)	1035.389	Bg(R)	1016.612	Bg	1050.2

Table 5 (Contd.)

(c) SbPO₄-type (BiPO₄-III)

Mode	LDA ω (cm ⁻¹)	Mode	PBESol ω (cm ⁻¹)	Modes	Exper. ω (cm ⁻¹)
Ag(R)	37.793	Ag(R)	38.294	Ag(R)	56.2
Ag(R)	72.050	Ag(R)	66.315	Ag(R)	68.8
Bg(R)	108.843	Bg(R)	103.842	Bg(R)	91.7
Ag(R)	129.424	Ag(R)	124.624		
Bg(R)	138.763	Ag(R)	132.830	Ag(R)	135.7
Ag(R)	140.465	Bg(R)	139.835	Bg(R)	144.5
Bg(R)	171.553	Bg(R)	166.922	Bg(R)	171.2
Ag(R)	200.240	Ag(R)	195.710	Ag(R)	214.2
Bg(R)	267.420	Bg(R)	258.022	Bg(R)	244
Bg(R)	326.328	Bg(R)	322.936	Bg(R)	353.6
Ag(R)	470.762	Ag(R)	463.573	Ag(R)	486.4
Ag(R)	508.221	Ag(R)	504.403	Ag(R)	548.3
Bg(R)	539.310	Bg(R)	533.724	Bg(R)	557.1
Ag(R)	582.139	Ag(R)	576.856	Ag(R)	609.9
Ag(R)	946.694	Ag(R)	929.982	Ag(R)	966.1
Bg(R)	955.200	Bg(R)	936.019	Bg(R)	982.9
Ag(R)	994.327	Ag(R)	978.050	Ag(R)	1037.8
Ag(R)	1035.589	Ag(R)	1017.946	Ag(R)	1046

BiPO₄-I.⁶⁰ The five modes observed at 944, 969, 980, 1012 and 1073 cm⁻¹ are assigned to the symmetric and asymmetric stretching frequencies of the P-O bonds of the PO₄ units of the trigonal phase. In a similar comparison with the earlier reported Raman modes of the PO₄ groups, the bands observed at 498, 546, 579 and 606 cm⁻¹ can be assigned to the bending (ν_4) modes and the bands at 379, 453 and 465 cm⁻¹ can be assigned to the (ν_2) bending modes of the PO₄ units. The stretching modes of the bonds in the PO₄ units in the monazite (II) phase are also quite similar to those observed for the trigonal (I) phase except for some splitting. This can be attributed to the highly dissimilar bond lengths in phases-I and II as described in the explanation of the IR results. Similar split bands are also observed at lower frequencies due to the internal modes of the BiO_n units of phase II and III. In particular phase II and III display an additional band around 400 cm⁻¹ compared to the trigonal (I) phase. Earlier, such a band was observed by Geng *et al.*⁵⁸ and Frost *et al.*⁶⁰ and had been assigned to the Bi-O stretching frequency of the BiO_n polyhedra. This intensity and shift in the frequencies can be assigned to the average Bi-O bond length and compactness of the polyhedra as the structure changes from trigonal to monazite-type or SbPO₄-type structures.

5. Conclusions

In summary, the detailed analyses of the powder X-ray and neutron diffraction data as well as IR and Raman studies on three polymorphs of BiPO₄ revealed accurate structural parameters and local distortions parameters around Bi³⁺ and P⁵⁺. Furthermore the structural parameters and vibrational frequencies were supported by *ab initio* calculations based on DFT. The irreversible trigonal-monazite-SbPO₄-type structural transitions are explained from the molar volume and total

energy of the three phases. The highly distorted structural arrangement around Bi³⁺ and P⁵⁺ has a very limited stability and is only stabilized by water molecules in the trigonal phase. It is revealed that the structural transition from the trigonal to monazite or SbPO₄ type structures is accompanied by a significant reduction in volume. DFT calculations revealed that the monazite and SbPO₄-type BiPO₄ have an almost similar total energy and hence a competing stability. Furthermore it is observed that the monazite type phase shows a larger lattice thermal expansion compared to the SbPO₄-type phase and thus it is truly a metastable phase.

Acknowledgements

This study was supported by the Spanish government MEC under grants no: MAT2010-21270-C04-01/04, by MALTA Consolider Ingenio 2010 project (CSD2007-00045), and by the Vicerrectorado de Investigación y Desarrollo of the Universidad Politécnica de Valencia (UPV2011-0914 PAID-05-11 and UPV2011-0966 PAID-06-11). S.N.A. acknowledges the support provided by Universitat de Valencia during his visit to it. A.M. and P.R.-H. acknowledge the computing time provided by Red Española de Supercomputación (RES) and MALTA-Cluster.

References

- 1 L. A. Boatner and B. C. Sales, in *Radioactive Waste Forms for the Future*, ed. W. Lutze and R. C. Ewing, North-Holland, Amsterdam, 1988, p. 495.
- 2 L. Bois, M. J. Guitter, F. Crrot, P. Trocellier and M. Gautier-Soyer, *J. Nucl. Mater.*, 2001, **297**, 129.

- 3 N. Dacheux, A. C. Thomas, V. Brandel and M. Genet, *J. Nucl. Mater.*, 1998, **257**, 108.
- 4 N. Clavier, N. Dacheux and N. Podor, *Inorg. Chem.*, 2006, **45**, 220.
- 5 N. Clavier, N. Dacheux, C. Wallez and M. Quarton, *J. Nucl. Mater.*, 2006, **352**, 209.
- 6 K. R. ELaud and F. A. Hummel, *J. Am. Ceram. Soc.*, 1971, **54**, 296.
- 7 O. Muller and R. Roy, *The Major Ternary Structural Families*, Springer, Berlin, 1974.
- 8 M. J. Kohn, J. Rakovan and J. M. Hughes, *Phosphates: Geochemical, Geobiological, and Materials Importance*, vol. 48, p. 87–123. (Ed), *Reviews in Mineralogy and Geochemistry*, Mineralogical Society of America and the Geochemical Society, Chantilly, Virginia, 2002.
- 9 D. Errandonea and F. J. Manjon, *Prog. Mater. Sci.*, 2008, **53**, 711.
- 10 O. Fukunaga and S. Yamaoka, *Phys. Chem. Miner.*, 1979, **5**, 167.
- 11 E. H. Oelkers and J.-M. Montel, *Elements*, 2008, **4**, 113.
- 12 G. J. McCarthy, W. B. White, R. Roy, B. E. Scheetz, S. Komarneni, S. K. Smith and D. M. Roy, *Nature*, 1978, **273**, 216.
- 13 G. J. McCarthy, W. B. White and D. E. Pfoertsch, *Mater. Res. Bull.*, 1978, **13**, 1239.
- 14 I.-S. Cho, G. K. Choi, J.-S. An, J.-R. Kim and K. S. Hong, *Mater. Res. Bull.*, 2009, **44**, 173.
- 15 N. Kitamura, K. Amezawa, Y. Tomii and N. Yamamotoa, *Solid State Ionics*, 2003, **161**, 162.
- 16 C. Pan, D. Li, X. Ma, Y. Chen and Y. Zhu, *Catal. Sci. Technol.*, 2011, **1**, 1399.
- 17 C. Pan, J. Xu, Y. Chen and Y. Zhu, *Appl. Catal., B*, 2012, **115**, 314.
- 18 M. Zhao, G. Li, J. Zheng, L. Li, H. Wang and L. Yang, *Cryst-EngComm*, 2011, **13**, 6251.
- 19 P. Arunkumar, C. Jayajothi, D. Jeyakumar and N. Lakshminarasimhan, *RSC Adv.*, 2012, **2**, 1477.
- 20 V. G. Alekseev, I. P. Gorelov and M. V. Kornilov, *J. Anal. Chem.*, 2005, **5**, 1055.
- 21 I.-S. Cho, J. R. Kim, D. W. Kim and K. S. Hong, *J. Electroceram.*, 2006, **16**, 379.
- 22 Z. Holgye and R. Poliak, *J. Radioanal. Nucl. Chem.*, 1991, **153**, 267.
- 23 Z. Holgye, *J. Radioanal. Nucl. Chem.*, 1998, **12**, 227.
- 24 C. Pan and Y. Zhu, *Environ. Sci. Technol.*, 2010, **44**, 5570.
- 25 C. Pan and Y. Zhu, *J. Mater. Chem.*, 2011, **21**, 4235.
- 26 R. C. L. Mooney-Slater, *Z. Kristallogr.*, 1972, **117**, 371.
- 27 G. Chiari and G. Ferraris, *Acta Crystallogr., Sect. B: Struct. Crystallogr. Cryst. Chem.*, 1982, **38**, 2331.
- 28 M. Roming and C. Feldmann, *J. Mater. Sci.*, 2009, **44**, 1412.
- 29 Y.-F. Lin, H.-W. Chang, S.-Y. Lu and C. W. Liu, *J. Phys. Chem. C*, 2007, **111**, 18538.
- 30 I.-S. Cho, J.-R. Kim, D.-W. Kim and K. S. Hong, *J. Electroceram.*, 2006, **16**, 379.
- 31 R. Masse and A. C. Durif, *C. R. Acad. Sci. Paris*, 1985, **300**, 349.
- 32 B. Romero, S. Bruque, M. A. G. Aranda and J. E. Iglesias, *Inorg. Chem.*, 1994, **33**, 1869.
- 33 B. S. Naidu, B. Vishwanadh, V. Sudarsan and R. K. Vatsa, *Dalton Trans.*, 2012, **41**, 3194.
- 34 M. Zhao, L. Li, J. Zheng, L. Yang and G. Li, *Inorg. Chem.*, 2013, **52**, 807.
- 35 A. C. Larson and R. B. van Dreele, *GSAS: General Structure Analysis System*, Los Alamos National Laboratory, Report LA-UR 86-748, 2000.
- 36 J. Rodriguez-Carvajal, *Fullprof 2000: A Program for Rietveld, Profile Matching and Integrated Intensity Refinements for X-ray and Neutron Data. Version 1.6*, Laboratoire Leon Brillouin, Gif sur Yvette, France, 2000.
- 37 G. Kresse and J. Furthmuller, *Phys. Rev. B: Condens. Matter*, 1996, **54**, 11169.
- 38 G. Kresse and D. Joubert, *Phys. Rev. B: Condens. Matter Mater. Phys.*, 1999, **59**, 1758.
- 39 P. E. Blochl, *Phys. Rev. B: Condens. Matter*, 1994, **50**, 17953.
- 40 J. P. Perdew and A. Zunger, *Phys. Rev. B*, 1981, **23**, 5048.
- 41 J. P. Perdew, K. Burke and M. Ernzerhof, *Phys. Rev. Lett.*, 1996, **77**, 3865.
- 42 A. Mujica, A. Rubio, A. Muñoz and R. J. Needs, *Rev. Mod. Phys.*, 2003, **75**, 863.
- 43 K. Parlinski, computer code PHONON [<http://wolf.ifj.edu.pl/phonon/>].
- 44 F. Xue, H. Li, Y. Zhu, S. Xiong, X. Zhang, T. Wang, X. Liang and Y. Qian, *J. Solid State Chem.*, 2009, **182**, 1396.
- 45 S. J. Patwe, S. N. Achary and A. K. Tyagi, *J. Mater. Res.*, 2009, **24**, 3551.
- 46 S. N. Achary, S. J. Patwe, M. D. Mathews and A. K. Tyagi, *J. Phys. Chem. Solids*, 2006, **67**, 774.
- 47 S. J. Patwe, S. N. Achary and A. K. Tyagi, *Am. Mineral.*, 2009, **94**, 98.
- 48 R. Lacombe-Perales, D. Errandonea, Y. Meng and M. Bettinelli, *Phys. Rev. B: Condens. Matter Mater. Phys.*, 2010, **81**, 064113.
- 49 V. Panchal, S. López-Moreno, D. Santamafía-Pérez, D. Errandonea, D. J. Manóon, P. Rodríguez-Hernandez, A. Muñoz, S. N. Achary and A. K. Tyagi, *Phys. Rev. B: Condens. Matter Mater. Phys.*, 2011, **84**, 024111.
- 50 D. Errandonea, R. S. Kumar, S. N. Achary and A. K. Tyagi, *Phys. Rev. B: Condens. Matter Mater. Phys.*, 2011, **84**, 224121.
- 51 L. Gracia, A. Beltran, D. Errandonea and J. Andres, *Inorg. Chem.*, 2012, **51**, 1751.
- 52 T. B. Zunic and L. Vickovic, *J. Appl. Crystallogr.*, 1996, **29**, 305.
- 53 E. Makovicky and T. B. Zunic, *Acta Crystallogr., Sect. B: Struct. Sci.*, 1998, **54**, 766.
- 54 M. E. Poloznikova and V. V. Fomichev, *Russ. Chem. Rev.*, 1994, **63**, 399.

- 55 L. Baia, R. Stefan, W. Kiefer, J. Popp and S. Simon, *J. Non-Cryst. Solids*, 2002, **303**, 379.
- 56 S. D. Ross, *Inorganic Infrared and Raman Spectra*, McGraw-Hill, London, 1972.
- 57 K. Nakamoto, *Infrared and Raman spectra of Inorganic and Coordination Compounds*, Wiley, New York, 1986.
- 58 J. Geng, W. H. Hou, Y. N. Lv, J. J. Zhu and H. Y. Chen, *Inorg. Chem.*, 2005, **44**, 8503.
- 59 G. M. Begun, G. W. Beall, L. A. Boatner and W. J. Gregor, *J. Raman Spectrosc.*, 1981, **11**, 273.
- 60 R. L. Frost, M. L. Weier, K. L. Erickson, O. Carmody and S. J. Mills, *J. Raman Spectrosc.*, 2004, **35**, 1047.